

Impurity Transport and Helium Accumulation in ITER

P. Leekhaphan

School of Bio-Chemical Engineering and Technology, Sirindhorn International Institute of Technology, Thammasat University, Klong Luang, Pathum Thani, 12121, Thailand

T. Onjun

School of Manufacturing Systems and Mechanical Engineering,
Sirindhorn International Institute of Technology,
Thammasat University, Klong Luang, Pathum Thani, 12121, Thailand
E-mail: thawatchai@siit.tu.ac.th

Abstract.

In this work, the behaviour of impurities, specifically the impurity transport and accumulation, in ITER plasma are predicted using 1.5D BALDUR integrated predictive modelling code. The impurity species considered are a combination of helium and beryllium. For each simulation, a linear combination of anomalous transport and neoclassical transport is used to describe the core plasma transport which consists of electron and ion thermal, hydrogenic, and impurity transports. The anomalous transport is self-consistently predicted using either the empirical Mixed Bohm/gyro-Bohm (Mixed B/gB) model or using the theory-based Multimode (MMM95) model; while the neoclassical transport is computed using the NCLASS model. Standard type I ELMy *H*-mode ITER discharges are simulated with and without the effects of sawtooth oscillations, which are predicted using the Porcelli sawtooth triggering model and a modified Kadomtsev magnetic reconnection model. It is found that, for the standard ITER scenario, helium and beryllium densities tend to accumulate inside the plasma. Both helium and beryllium densities quickly rise and level off to steady-state values, which depend sensitively on their values at the boundary. However, sawtooth oscillation has a strong impact on suppression of the impurity accumulation for both helium and beryllium. A sensitivity study is also carried out to determine the impacts of changing the impurity transport coefficient, edge effective charge, line-averaged density, and edge helium density. It is found that increasing the impurity transport coefficient results in the reduction of steady-state values of helium and beryllium densities, but has minor influence over temperature and ion plasma densities. On the other hand, increasing the edge effective charge greatly increases the beryllium density, but has small impact on other species. Both helium and beryllium densities are found to be heavily dependent on boundary helium density, but are weakly dependent on line-averaged density.

Keyword: Impurity Transport, Helium Accumulation, ITER

1. Introduction

Although magnetically-confined thermonuclear fusion has recently received significant attention as a potential environ-

mentally-benign power generation method, its technical and engineering feasibility has yet to be demonstrated. Consequently, an international project called the International Thermonuclear Experimental Reactor

(ITER) was officially initiated in 2006 [1]. The main goal of the ITER project is to achieve a continuous and sustained nuclear fusion reaction based on deuterium and tritium, *i.e.* burning plasma, for approximately 1 hour. As ITER is expected to operate over an extended period of time, a feat hitherto unachieved in present-day tokamaks, there are several concerns that are of particular interest. One of the most important concerns is the impurity behaviour in the plasma, especially the accumulation of helium ash because of the retention of the inevitable helium ash or alpha particles generated from the D-T nuclear fusion reaction. The accumulation of impurities in plasmas can result in fuel dilution, enhancement of core radiation, and, consequently, degradation of fusion performance [2]. It is, therefore, crucial to investigate the impurity behaviour in ITER, especially the impurity transport and accumulation.

Impurity accumulation in the confinement-enhanced *H*-mode plasma, as would be expected in ITER, has long been anticipated. In fact, at the conceptual stage of the ITER project, one of the major questions was whether ITER can achieve enhanced confinement and sufficient helium exhaust simultaneously [3]. Several experiments were designed to answer this question, and have confirmed an affirmative answer [4]. A comprehensive review of experiments on helium accumulation and exhaust can be found in Ref. [4]. Various simulations of ITER cases have also been conducted to study impurity accumulation in ITER, especially that of helium ash. Kamelander *et al.* [5] carried out simulations on ITER-like cases using 1.5D transport code, and found that temperature and helium density reach steady-state values under an appropriate burn control system. Recent work by Onjun *et al.* [6] also indicates quasi-steady state density of helium, as well as that of beryllium. A more comprehensive integrated modelling of ITER reference scenarios can be found in

Ref. [7], where various issues concerning ITER operations are addressed. However, impurity behaviour studied in the paper focused on higher-Z impurities, such as argon and tungsten, and the accumulation of helium was not described. Fichtmüller *et al.* [8] carried out simulations of ITER plasmas that combine both core plasma transport and impurity exhaust by divertor using Combined Code Numerical Utility for Tokamaks (COCONUT), coupled with EDGE2D/NIMBUS code. This approach is an excellent attempt at global impurity simulation, although it requires that background plasma be ‘frozen’ to let a scrape-off layer evolve, as well as extensive computing power. The mechanisms of impurity transport have been investigated by Fülöp *et al.* [2, 9], where the impacts of anomalous and neoclassical impurity transport for ITER-like plasmas are studied.

The present study aims to predict, via self-consistent simulations, the profiles of helium and beryllium densities, as well as their time evolution, in type I ELMy *H*-mode ITER discharges. This will be done with and without considering the effects of sawtooth oscillation, which is expected to have a strong impact on an impurity accumulation. Although there are a number of discussions suggesting that the plasma wall and divertors in ITER should be made of tungsten rather than beryllium, in this work, it is assumed that the impurities are a combination of helium and beryllium, which is similar to present-day tokamaks. In addition, a parametric sensitivity study is carried out to determine the impacts of impurity particle transport coefficient, edge effective charge, line-averaged density, and ratio of edge helium density to electron density.

This paper is organized as follows: brief descriptions of relevant components of the BALDUR code, including the anomalous transports and pedestal models, are given in section 2; the predictions of ITER plasma profiles for standard type I ELMy

H-mode are presented and discussed in section 3; sensitivity analysis is found in section 4; and a summary is given in section 5.

2. BALDUR integrated predictive modelling code

The BALDUR integrated predictive modelling code [10] has been widely utilized to calculate the time evolution of various plasma properties, including electron and ion temperatures, deuterium and tritium densities, helium and impurity densities, safety factor, neutrals, and fast ions. Various physical processes incorporated in the code are: transport, plasma heating, helium influx, boundary conditions, plasma equilibrium shape, and sawtooth oscillations. The models for each process are combined to self-consistently solve for plasma properties. BALDUR code predicts fusion heating and helium ash accumulation via the nuclear fusion rate, coupled with the Fokker Planck package used to calculate the slowing down of the spectrum of fast alpha particles on each flux surface. Also, the fusion heating component of the BALDUR code calculates the production rate of thermal helium ions and the rate of the depletion of deuterium and tritium ions within the plasma core. Simulation results obtained from BALDUR code have previously been compared with experimental data, yielding an overall agreement of approximately 10% relative RMSE deviation [11, 12].

2.1 Multimode core transport model (MMM95)

The Multi-Mode Model version 1995 (MMM95) [13] is a combination of theory-motivated transport models used to predict plasma profiles in tokamaks. It consists of the Weiland model for the ion temperature gradient (ITG) and trapped electron modes (TEM), the Guzdar–Drake model for drift-resistive ballooning modes,

and kinetic ballooning modes. Usually, the Weiland model for drift modes provides the largest contribution, followed by the drift-resistive ballooning mode and the kinetic ballooning mode respectively. The Weiland model (χ_{Weiland}) is derived by linearizing the fluid equations, with magnetic drifts for each plasma species. Eigenvalues and eigenvectors computed from these fluid equations are then used to compute a quasi-linear approximation for the thermal and helium transport fluxes. The Weiland model includes many different physical phenomena such as effects of trapped electrons, unequal ion and electron temperatures, impurities, fast ions, and finite β . The resistive ballooning model (χ_{RB}) in the MMM95 transport model is based on the 1993 *ExB* drift-resistive ballooning mode model by Guzdar–Drake, in which the transport is proportional to the pressure gradient and collisionality. The contribution from the resistive ballooning model usually dominates the transport near the plasma edge. The kinetic ballooning model (χ_{KB}) is a semi-empirical model, which usually provides a small contribution to the total diffusivity throughout the plasma, except near the magnetic axis. However, for the ITER cases in this work, it is found that the contribution from the kinetic ballooning mode plays quite a significant role in the region near the plasma core up to a radius of 1.0 m. This will be discussed in Section 3. This model is an approximation to the first ballooning mode stability limit. All the anomalous transport contributions to the MMM95 transport model are multiplied by κ^4 since the models were originally derived for circular plasmas. The expressions of transport coefficients in MMM95 are:

$$\chi_i = 0.8\chi_{\text{Weiland}} + 1.0\chi_{\text{RB}} + 1.0\chi_{\text{KB}} \quad (1)$$

$$\chi_e = 0.8\chi_{\text{Weiland}} + 1.0\chi_{\text{RB}} + 1.0\chi_{\text{KB}} \quad (2)$$

$$D_H = 0.8\chi_{\text{Weiland}} + 1.0\chi_{\text{RB}} + 1.0\chi_{\text{KB}} \quad (3)$$

$$D_Z = C_{\text{imp}} (0.8\chi_{\text{Weiland}} + 1.0\chi_{\text{RB}} + 1.0\chi_{\text{KB}}) \quad (4)$$

where C_{imp} is a constant of proportionality for impurity transport. Although it may be varied (as will be discussed in section 4), C_{imp} is taken as 1.0 in standard cases. Note that the notations used in this paper are given in Table 1.

2.2 Mixed B/gB core transport model

The Mixed B/gB core transport model [14] is derived empirically. The model started off as a local transport model with Bohm scaling, where the transport fluxes depend entirely on local plasma properties and the transport diffusivities are proportional to the gyro-radius multiplied by thermal velocity over a plasma linear dimension such as major radius. Transport diffusivities in models with Bohm scaling are functions of the profile shapes (characterized by normalized gradients) and other plasma parameters such as magnetic q , which are all assumed to be held fixed in systematic scans in which only the gyro-radius is changed relative to plasma dimensions. The model was originally developed for JET plasmas, and was later extended to describe ion transport, and a gyro-Bohm term was added in order to improve predictions of plasmas in smaller tokamaks as well as larger machines. A transport model is said to have ‘gyro-Bohm’ scaling when the transport diffusivities are proportional to the square of the gyro-radius multiplied by thermal velocity over the square of the plasma linear dimension. Usually, the Bohm term provides a larger contribution than the gyro-Bohm term, which normally exhibits a large contribution in the deep core of the plasma, and plays a significant role only in smaller tokamaks with relatively low power and magnetic field.

In the Mixed B/gB core transport, both the electron and ion thermal diffusivities consist of two terms, one with Bohm scaling and the other with gyro-Bohm scaling:

$$\chi^{\text{B}} \equiv \rho_s c_s q^2 \frac{a}{p_e} \frac{dp_e}{dr} \Delta T_e \quad (5)$$

$$\chi^{\text{gB}} = \frac{\rho_s^2 c_s}{T_e} \frac{dT_e}{dr} \quad (6)$$

In the Bohm diffusivity expression, ΔT_e is a finite difference approximation to the normalized temperature electron temperature difference at the plasma edge, given by:

$$\Delta T_e = \frac{[T_e]_{r/a=0.8} - [T_e]_{r/a=1.0}}{[T_e]_{r/a=1.0}} \quad (7)$$

The anomalous ion and electron thermal diffusivities are obtained by taking a linear combination of the Bohm and gyro-Bohm term, with coefficients that are determined empirically:

$$\chi_i = 1.6 \times 10^{-4} \chi^{\text{B}} + 1.75 \times 10^{-2} \chi^{\text{gB}} \quad (8)$$

$$\chi_e = 8.0 \times 10^{-5} \chi^{\text{B}} + 3.5 \times 10^{-2} \chi^{\text{gB}} \quad (9)$$

The hydrogenic and impurity charged helium diffusivities are given by:

$$D_H = \frac{\chi_e \chi_i}{\chi_e + \chi_i} \quad (10)$$

$$D_Z = D_H \quad (11)$$

2.3 Pedestal model

In the development of the pedestal temperature model described in Ref. [15], the pedestal width (Δ) and the pressure

gradient ($\partial p/\partial r$) are required. If the pedestal density (n_{ped}) is known, the temperature at the top of the pedestal (T_{ped}) can be estimated as:

$$T_{\text{ped}} = \frac{\Delta}{2kn_{\text{ped}}} \left| \frac{\partial p}{\partial r} \Delta \right| = \frac{\Delta}{2kn_{\text{ped}}} \frac{\alpha_c B_\phi^2}{2\mu_0 Rq^2} \quad (12)$$

These pedestal temperature models yield equally satisfactory agreement with the pedestal data from the ITPA Pedestal Database. The pedestal temperature models are based on the magnetic and flow shear stabilization width scaling ($\Delta \propto \rho_s^2$), based on the flow shear stabilization width scaling

($\Delta \propto \sqrt{\rho Rq}$), or based on the normalized poloidal pressure width scaling

($\Delta \propto R\sqrt{\beta_{\theta, \text{ped}}}$). The pedestal pressure gradient calculation is normally complicated and requires detailed inputs. For simplicity, the pedestal gradient is assumed to be uniform throughout the pedestal region and the pedestal gradient is limited by the first stability limit of infinite n ballooning mode, so that the normalized critical pressure gradient for the pedestal region is estimated by:

$$\alpha_c = -\frac{2\mu_0 Rq^2}{B_\phi^2} \left(\frac{\partial p}{\partial r} \right)_c = 0.4s \left[1 + \kappa_{95}^2 (1 + 5\delta_{95}^2) \right] \quad (13)$$

where κ_{95} is the elongation at the 95% flux surface, and δ_{95} is the triangularity at the 95% flux surface. It is worth noting that these pedestal temperature models were derived from different pedestal width scalings. The pedestal width constant in each model was chosen to minimize the RMS deviation with 533 experimental data points from 4 large tokamaks obtained from the International Tokamak Physics Activity (ITPA) pedestal database. In this work, the

pedestal models with the chosen width constant in Ref. [15] are used. These pedestal temperature models include the effect of edge bootstrap current, which has an impact on magnetic shear and safety factor. This inclusion results in a non-linear behaviour in the pedestal temperature model. The scheme to deal with the approximation of magnetic shear and safety factor for the pedestal prediction using the pedestal models was completely described in Ref. [15]. Therefore, the values of magnetic shear and safety factor for the pedestal calculation are different from their values in other parts of the BALDUR code, which are based on a simpler calculation. The attempt to use a self-consistent safety factor and magnetic shear for all calculations in BALDUR code is under development. A preliminary result can be seen in Ref. [16]. In addition, there are several new approaches to estimate pedestal value, such as the pedestal scaling by M. Sugihara [17], which predicted the pedestal temperature of about 5.6 keV.

The density at the top of the pedestal is described by a simple empirical model that assumes proportionality between pedestal density and line-averaged density. Since the pedestal density, n_{ped} , is usually a large fraction of line average density, n_l , the pedestal density can be calculated as:

$$n_{\text{ped}} = 0.71n_l \quad (14)$$

This pedestal density model agrees with the pedestal data obtained from the ITPA pedestal database with 12% RMSE [18]. In this work, it is assumed that the impurity consists of helium and beryllium. It is worth mentioning that other species of impurities such as carbon or tungsten can be involve. The ratio of helium to electron density at the edge is assumed to be 2%. The effective charge is 1.4 at the edge of the plasma. With these conditions, the density of helium can be computed. The densities of helium and beryllium at the top of the

pedestal are 5.68×10^{18} and $1.42 \times 10^{18} \text{ m}^{-3}$, respectively.

3. Simulation results and discussion

The simulations are carried out using 1.5D BALDUR integrated predictive modelling code. Physical parameters are chosen to match those of type I ELMy *H*-mode ITER discharges ($R = 6.2 \text{ m}$, $a = 2.0 \text{ m}$, $I_p = 15 \text{ MA}$, $B_T = 5.3 \text{ T}$, $\kappa_{95} = 1.7$, $\delta_{95} = 0.33$, $n_1 = 1.0 \times 10^{20} \text{ m}^{-3}$ and $Z_{\text{eff,edge}} = 1.4$). The simulations are carried out from the centre to the top of the pedestal. The pedestal area is described by the model in section 2.3. The total auxiliary heating power used in the simulations is 40 MW, of which 33 MW comes from NBI heating power and 7 MW comes from RF heating power. The plasma current and density are slowly ramped up to the target values within the first 100 seconds of the simulations. During the start-up phase, the plasma current was initially 3 MA, and it is slowly increased to the target value of 15 MA. It should be noted that several physical processes are not included in these simulations, such as ELM crashes and neoclassical tearing modes. Hence, the simulation results do not represent the complete ITER plasma dynamics. However, it is expected that these simulations include sufficient physics to describe the plasma when it reaches a quasi-steady state. For each simulation, anomalous transport is calculated either using an empirical Mixed B/gB core transport model or using a theory-based MMM95 core transport model while neoclassical transport is computed using the NCLASS module. The boundary conditions are provided at the top of the pedestal by the pedestal model. An assumption made in the present BALDUR code is equal ion and electron temperatures at the pedestal. It has been observed in many experiments that ion temperature is higher than electron temperature at the pedestal in low density plasma. As ITER plasma is

high density plasma, the assumption of temperature equality in BALDUR code is expected to be valid. Previous ITER simulations using the JETTO code in Ref. [19] gave electron and ion temperatures at the top of the pedestal of 4.4 and 4.9 keV, respectively. The assumption of equal ion and electron temperature employed by BALDUR code has been used to simulate present-day *H*-mode experiments. The results yield 10% RMS deviation from the experiments [18]. In this work, unless denoted otherwise, the simulation results represent cases where pedestal width scaling based on magnetic and flow shear stabilization is used.

Figures 1 and 2 show the profiles of ion temperature, electron temperature, ion density, electron density, deuterium density, tritium density, helium density, and beryllium density obtained from the simulations as functions of normalized minor radius at different times of the simulations. These simulations are carried out either using an empirical anomalous core transport Mixed B/gB model or a theory-based MMM95 core transport model. The boundary conditions in these simulations are predicted using the pedestal model based on the magnetic and flow shear stabilization width scaling. As mentioned, the value of C_{imp} is set to be 1.0. It can be seen that all temperature and density profiles evolve and reach a quasi-steady state. As the line-averaged density is set to reach target density at 100 sec, it is expected that the ion, electron, deuterium, tritium, and beryllium densities tend to reach steady state before 100 sec, as these species are not products of the reaction. On the other hand, ion and electron temperatures, and helium density tends to reach steady-state after 100 sec, as they are dependent on the rate of the reaction. The density profiles of ions, electrons, deuterium and tritium are noticeably flatter than those of helium and beryllium. As a species is said to be accumulated in the plasma when its density

profile is more peaked than the main plasma ion density [20], it can be concluded that the simulations show helium and beryllium accumulation in the plasmas. Also, the density of helium is larger than that of beryllium. This is expected as helium is continually produced from the deuterium and tritium (D-T) nuclear fusion reactions, while beryllium is produced at the edge. It should be noted that the model for production of beryllium through first-wall sputtering is not fully integrated into BALDUR code. In this work, the edge beryllium density and helium density are fixed via specifying a constant edge effective charge ($Z_{\text{eff,edge}}$). Although the characteristics of sputtering, such as temperature dependence, are not considered, it is assumed that fixing edge beryllium density gives sufficiently similar effects. The results obtained using Mixed B/gB and MMM95 core transport models show similar trends. However, MMM95 predicts larger ion and electron temperature, particle build-up near the edge for all species, and slower profile evolution. The density peaks near the plasma edge are characteristic to MMM95, and are documented in Ref. [16].

Since impurity accumulation in the plasma core enhances core radiation, it is particularly undesirable. Hence, attention will be given to the time evolution of central density of helium ($n_{\text{He,o}}$) and beryllium ($n_{\text{Be,o}}$), as well as radiative power loss (P_{rad}) and total alpha heating power ($P_{\alpha,\text{total}}$), shown in Figure 3. Both Mixed B/gB and MMM95 predict central helium and beryllium density to quickly increase and level off to quasi-steady state values. It is observed that the MMM95 model predicts larger quasi-steady state central helium density than the Mixed B/gB core transport model. This is expected since MMM95 predicts larger total alpha heating power than Mixed B/gB, which corresponds to faster D-T nuclear fusion rate, and, therefore, faster production rate of helium.

Also, radiative power loss predicted by MMM95 is larger than that predicted by Mixed B/gB because of larger central helium density. Simulation results of standard cases using different pedestal width scaling are given in Table 2 for the Mixed B/gB core transport model and Table 3 for the MMM95 core transport model. It is found that all three pedestal width scalings give similar results.

Figure 4 shows the ion (χ_i) and electron (χ_e) thermal transport coefficients, and hydrogenic (D_H) and impurity (D_Z) transport coefficients as functions of normalized minor radius at various times. All profiles evolve and reach quasi-steady state values in these simulations. It is found that MMM95 gives a slightly larger D_Z than Mixed B/gB. Also, MMM95 predicts a larger D_H , and a smaller χ_i and χ_e than the Mixed B/gB core transport model, accounting for the observation of larger ion and electron temperatures, and smaller deuterium and tritium densities, when the core transport model was switched from the Mixed B/gB to MMM95 model (Figures 1 and 2).

Contributing terms in ion thermal and impurity transport coefficients as functions of normalized minor radius are found in figure 5. For the Mixed Bohm/gyro-Bohm core transport model, it is observed that the Bohm term provides the major contribution in most regions of the plasma, while the gyro-Bohm term provides significant contribution only near the center, and neoclassical transport is almost negligible. This is consistent with Refs. [14] and [2]. For the MMM95 core transport model, the Weiland term provides the greatest contribution to χ_i (similar trend is observed for χ_e), while the kinetic-ballooning term provides the greatest contribution to D_Z (similar trend is observed for D_H). The large contribution from the Weiland model for χ_i has been reported in previous simulations [11-12].

Even though BALDUR simulation cannot fully describe the dynamics of plasma evolution during the current phase, it should be sufficient to describe plasma dynamics during the quasi-steady state, especially the sawtooth oscillation, which was identified as one of the most fundamental dynamics of ITER plasmas [1]. In this study, the Porcelli sawtooth triggering model [21] is used to predict sawtooth crashes and a modified Kadomtsev magnetic reconnection model [22] is used to calculate the response of plasma after each crash. It is found that ion and electron temperatures, and ion, electron, deuterium, tritium, helium and beryllium densities reach quasi-steady state values. The values of central ion and electron temperatures, as well as the density of all species before and during sawtooth crash, and those obtained from simulations without sawtooth crash, can be found in Table 4 for Mixed B/gB and Table 5 for the MMM95 core transport model. When sawtooth oscillation is included, it is observed that ion and electron temperatures decrease greatly. Also, helium density drops significantly, and beryllium density decreases slightly. The observation is consistent with conventional wisdom that sawtooth oscillations can prevent the accumulation of impurities [23]. Ion, electron, deuterium and tritium density remain almost unchanged, as BALDUR controls them by means of automatic gas puffing. During sawtooth crashes, it is seen that ion and electron temperatures, as well as ion, electron, deuterium and beryllium densities, drop slightly, whereas tritium and helium densities actually increase during sawtooth crash. This is probably due to the enhancement of collisionality when temperature is lowered, as documented in Ref. [18].

4. Sensitivity Study

In this section, the parametric sensitivity of BALDUR simulation results is investigated. The effects of varying impurity transport coefficient (D_Z), edge effective charge ($Z_{\text{eff,edge}}$), line-averaged density (n_l), and ratio of beryllium density to electron density at the edge ($n_{\text{Be,edge}}/n_{e,\text{edge}}$) are studied and discussed in sections 4.1 to 4.4, respectively. Note that in this section, only the MMM95 core transport model will be used to carry out the simulations.

4.1 Effect of varying D_Z

In this study, the impacts of D_Z are investigated by varying the coefficient C_{imp} (Eqn. 4). As the value of C_{imp} is varied, it is expected that the impurity transport would differ from the trends observed in section 3. In this study, simulations are carried out using C_{imp} values of 0.5, 1.0 and 2.0. As in section 3, all profiles of transport coefficients and plasma properties obtained from simulations are observed to reach quasi-steady state. Therefore, only the quasi-steady state profiles will be considered.

The profiles of χ_i , χ_e , D_H and D_Z from each simulation are shown in Figure 6. It can be seen that χ_i , χ_e and D_H are almost unchanged, and only the values of D_Z are varied. Hence, any change in predicted plasma behaviours can be attributed to the variation in D_Z .

The time evolution of central ion temperature and helium density, as well as radiative power loss and total alpha heating power, are presented in Figure 7. It is seen that the quasi-steady state value of central helium density is largest when C_{imp} of 0.5 is used, followed by C_{imp} of 1.0 and 2.0., respectively. This is expected since suppressed transport ($C_{\text{imp}}=0.5$) would lead to enhanced impurity accumulation. Also, since impurity accumulation corresponds directly to the radiated power, radiative power loss increases with decreasing C_{imp} .

On the other hand, ion temperature and total alpha heating power decrease with decreasing D_Z ($C_{imp} = 0.5$). This is, again, expected since impurity accumulation, which is enhanced when C_{imp} of 0.5 is used, tends to suppress nuclear fusion reaction by diluting the fuels. Although not shown graphically here, it is observed that all other profiles show small changes when C_{imp} is varied.

4.2 Effect of varying $Z_{eff,edge}$

In 1.5D simulation, it is necessary to specify boundary density for all species. In this work, the densities of deuterium, tritium, and beryllium are specified at the top of the pedestal, whereas boundary beryllium density is calculated from the edge effective charge $Z_{eff,edge}$. The standard value of $Z_{eff,edge}$ used in section 3 is 1.4, which represents optimistically a 'clean' near-wall region. Hence, in this section, we carry out a sensitivity study to determine the effect of increasing $Z_{eff,edge}$ in order to simulate scenarios when there is a larger amount of impurity in the near-wall region. In this study, the values of $Z_{eff,edge}$ used in simulations are 1.4, 1.7 and 2.0.

The quasi-steady state profiles of ion thermal transport coefficient and impurity particle transport coefficient as functions of normalized minor radius are presented in Figure 8. Note that the value of transport shown in the figure is only from 0 to 2 m²/s. It is observed that a larger $Z_{eff,edge}$ value generally gives smaller χ_i and D_Z . Figure 9 shows the time evolution of central ion temperature, central helium density, radiative power loss and total alpha heating power. It can be seen that larger $Z_{eff,edge}$ gives rise to smaller $T_{i,o}$, due to fuel dilution. It is also observed that central helium density and radiative power loss increase with increasing $Z_{eff,edge}$, because they are directly related, *i.e.* the larger the effective charge, the larger the radiation and density of the product. On the other hand, total alpha heating power is observed to

drop when $Z_{eff,edge}$ is increased. However, it should be noted that fixing boundary beryllium density and calculating boundary beryllium density is not an entirely realistic approach, since boundary helium density cannot be controlled in an actual tokamak. The effects of increasing helium density are discussed in section 4.4.

4.3 Effect of varying n_1

Impurity transport depends on a number of factors such as plasma temperature, line-averaged density and the nature of impurity species. Since line-averaged density is a parameter that can be easily monitored and controlled in actual tokamak operation, it would be interesting to find out if impurity accumulation can be enhanced or hindered, *i.e.* controlled, merely by varying the plasma density. The target line-averaged density can normally be achieved either using gas puffing or using pellet injection. The standard ITER simulations in section 3 use a line-averaged density of $1.0 \times 10^{20} \text{ m}^{-3}$. In this section, simulations are carried out using n_1 of 0.8, 1.0 and $1.2 \times 10^{20} \text{ m}^{-3}$.

The time evolution of central ion temperature, central helium density, radiative power loss and total alpha heating power are shown in Figure 10. It can be seen that, apart from central ion temperature, all other variables appear to decrease when a smaller n_1 is used. Central T_i is observed to increase when n_1 is decreased. This is evident if the ideal gas law is considered. Assuming plasma pressure is relatively constant, smaller density corresponds to larger temperature. Time evolution of core helium density, radiative power loss and total alpha heating power show the opposite trend, with smaller n_1 corresponding to smaller values of the density and power. This can be accounted for by considering deuterium and tritium density. When n_1 is small, both deuterium and tritium density are small, leading to reduced fusion rate, helium production, and total

alpha heating power. Consequently, radiative power loss drops as there is a smaller amount of impurity. In short, the amount of impurity and radiative power loss can be reduced by decreasing n_i , but at the price of decreased alpha heating power.

4.4 Effect of varying $n_{\text{Be,edge}}/n_{\text{e,edge}}$

As mentioned earlier, BALDUR requires that the boundary density of all species be specified in order to carry out simulations. In this study, the boundary helium density is specified by fixing the edge beryllium density to edge electron density ratio ($n_{\text{Be,edge}}/n_{\text{e,edge}}$). The ratio is 2% in standard cases, found in section 3. In this part, the effect of varying the ratio is investigated. Simulations are carried out with $n_{\text{Be,edge}}/n_{\text{e,edge}}$ values of 1%, 2% and 3%.

Figure 11 presents the time evolution of central ion temperature, central helium density, radiative power loss and total alpha heating power. Since central helium density depends on boundary helium density, it is not surprising to find that the central helium density and total alpha heating power are heavily dependent on $n_{\text{Be,edge}}/n_{\text{e,edge}}$. Increasing $n_{\text{Be,edge}}/n_{\text{e,edge}}$ leads to reduced central helium density and total alpha heating power due to dilution by beryllium. Central ion temperature obtained from simulations does not seem to be heavily dependent on $n_{\text{Be,edge}}/n_{\text{e,edge}}$. Also, it is observed that radiative power loss increases with increasing $n_{\text{Be,edge}}/n_{\text{e,edge}}$. It can be concluded that simulation results are heavily dependent on $n_{\text{He,edge}}/n_{\text{e,edge}}$. However, fixing edge helium density is not an entirely realistic approach since helium is continually produced and removed, and there is no means of fixing its density at the edge in actual operation. Therefore, it would be desirable to develop a simple model that relates boundary helium density to core helium density in order to provide BALDUR with more realistic boundary conditions.

5. Conclusions

In the present study, the behaviours of impurity transport and accumulation in type I ELMy H -mode ITER discharges are investigated via simulations using 1.5D BALDUR integrated predictive modelling code. The impurity species considered are a combination of helium and beryllium. The simulations are carried out using either the Mixed B/gB or MMM95 core transport model, coupled with the NCLASS neo-classical model and pedestal model. It is found that ion and electron temperatures, as well as ion, electron, deuterium, tritium, helium and beryllium densities reach quasi-steady state values. The inclusion of sawtooth oscillation is observed to suppress core impurity density, particularly for helium. In the parametric sensitivity analysis, the impacts of impurity particle transport coefficient, edge effective charge, line-averaged density, and edge helium density to electron density ratio are investigated. All four parameters are observed to influence impurity behaviours.

6. Acknowledgments

The authors are grateful to Prof. A H Kritz, Dr. G Bateman, Dr. V Parail, Dr. A Pankin, Dr. S Suwanna, Dr. N Poolyarat, Dr. R Picha, Mr. T Pralongkij, and Mr. T J Downey for their helpful discussions and support. This work is supported by the Commission on Higher Education (CHE) and the Thailand Research Fund (TRF) under Contract No. RMU5180017, and the Thailand National Research University Project.

7. References

- [1] Aymar R., Barabaschi P. and Shimomura Y., *Plasma Phys. Controlled Fusion*, Vol. 44, pp. 519-65, 2002.

- [2] Fülöp T. and Weiland J., *Phys. Plasmas*, Vol. 13, 112504, 2006.
- [3] Post D, Cohen S, ITER Physics Group and IAEA , *ITER Physics*, 1990.
- [4] Hogan J., *J. of Nucl. Mater.*, Vol. 241-3, pp. 68-81, 1997.
- [5] Bürbaumer H., Kamelander G., Sigmar D. J. and Wising F., *Fusion Tech.*, Vol. 35, pp. 280-8, 1999.
- [6] Onjun T. and Pianroj Y., *Nucl. Fusion*, Vol. 49, 075003, 2009.
- [7] Parail V, *et al.*, *Nucl. Fusion*, Vol. 49, 075030, 2009.
- [8] Fichtmüller M., Corrigan G., Lauro-Taroni L., Simonini R., Spence J., Springmann E. and Taroni A., *J. of Nucl. Mat.*, Vol. 266-9, pp. 330-6, 1999.
- [9] Fülöp T. and Nordman H., *Phys. Plasmas* , Vol. 16, 032306, 2009.
- [10] Singer C E, *et al.*, *Comput. Phys. Commun.*, Vol. 49, pp. 275-398, 1988.
- [11] Hannum D, Bateman G, Kinsey J, Kritz A. H., Onjun T. and Pankin A., *Phys. Plasmas*, Vol. 8, p. 964, 2001.
- [12] Onjun T., Bateman G., Kritz A. H. and Hannum D., *Phys. Plasmas*, Vol. 8, p. 975, 2001.
- [13] Bateman G., Kritz A. H., Kinsey J. E., Redd A. J. and Weiland J., *Phys. Plasmas*, Vol. 5, pp. 1793-99, 1998.
- [14] Erba N., Cherubini A., Parail V., Springmann E. and Taroni A., *Plasma Phys. Controlled Fusion*, Vol. 39, pp. 261-77, 1997.
- [15] Onjun T., Bateman G. and Kritz A. H. , *Phys. Plasmas*, Vol. 9, pp. 5018-30, 2002.
- [16] Onjun T., Tharasrisuthi K., Pankin A. Y. and Onjun T., *J. of Physics: Conference Series*, Vol. 123, 012034, 2008.
- [17] Sugihara M., Mukhovatov V., Polevoi A. and Shimada M., *Plas. Phys. Cont. Fusion*, Vol. 45 L55, 2003.
- [18] Bateman G., Onjun T. and Kritz A. H., *Plas. Phys. Cont. Fusion*, Vol. 45, 1939-60, 2003.
- [19] Onjun T., Kritz A. H., Bateman G. and Parail V., *Phys. Plasmas*, Vol. 12, 082513, 2005.
- [20] Dux R., Giroud C., Neu R., Peeters A. G., Stober J., Zastrow K-D and Contributors to the EFDA-JET Workprogramme ASDEX Upgrade Team, *J. of Nucl. Mater.* Vol. 313-6 , pp. 1150-5, 2003.
- [21] Houlberg W. A., Shaing K. C., Hirshman S. P. and Zarnstorff M. C., *Phys. Plasmas*, Vol. 4, pp. 3231,1997.
- [22] Porcelli F., Boucher D. and Rosenbluth M. N., *Plasma Phys. Controlled Fusion*, Vol. 38, pp. 2163-86, 1996.
- [23] Mukhovatov V, *et al.*, *Plas. Phys. Cont. Fusion* , Vol. 4, pp. A235-52, 2003.

8. List of Tables

Table 1: Notation used in this paper.

Table 2: Summary of plasma properties obtained from simulations using Mixed B/gB core transport model, coupled with pedestal width model based on magnetic and flow shear stabilization, flow shear stabilization, and normalized poloidal pressure scalings.

Table 3: Summary of plasma properties obtained from simulations using MMM95 core transport model, coupled with pedestal width model based on magnetic and flow shear stabilization, flow shear stabilization, and normalized poloidal pressure scalings.

Table 4: Quasi-steady state values of central ion and electron temperatures, and densities of ion, electron, deuterium, tritium, helium and beryllium. The values are taken from simulations without sawtooth oscillation,

and simulations with sawtooth oscillation before and during sawtooth crash. Mixed B/gB core transport model is used.

Table 5: Quasi-steady state values of central ion and electron temperatures, and densities of ion, electron, deuterium, tritium, helium and beryllium. The values are taken from simulations without sawtooth oscillation, and simulations with sawtooth oscillation before and during sawtooth crash. MMM95 core transport model is used.

9. List of Figures

Figure 1: Profiles of ion and electron temperatures, and densities of ion, electron, deuterium, tritium, helium, and beryllium at 10, 100, 1000, and 3000 sec. The profiles are obtained from simulations using Mixed B/gB core transport model.

Figure 2: Profiles of ion and electron temperatures, and densities of ion, electron, deuterium, tritium, helium, and beryllium at 10, 100, 1000, and 3000 sec. The profiles are obtained from simulations using MMM95 core transport model.

Figure 3: Time evolution of central helium and beryllium densities, radiative power loss and total alpha heating power are shown. The results are obtained from the simulations using either Mixed B/gB or MMM95 core transport models.

Figure 4: Profiles of ion and electron thermal transport coefficients (χ_i and χ_e), and hydrogenic and impurity transport coefficients (D_H and D_Z) obtained from Mixed B/gB (left panels) and MMM95 (right panels) core transport models are shown.

Figure 5: Contributing terms in ion thermal transport coefficients (χ_i) and impurity particle transport coefficient (D_Z) calculated using Mixed B/gB and MMM95 core

transport models are shown as functions of normalized minor radius.

Figure 6: Profiles of ion and electron thermal transport coefficients (χ_i and χ_e), and hydrogenic and impurity particle transport coefficients (D_H and D_Z) obtained from simulations using Mixed B/gB and MMM95 core transport models, with $C_{imp}=0.5, 1.0, 2.0$, are shown.

Figure 7: Time evolution of central ion temperature, central helium density, radiative power loss and total alpha heating power upon varying the constant C_{imp} are shown. The results are obtained from simulations using MMM95 core transport model, with C_{imp} of 0.5, 1.0, and 2.0.

Figure 8: Profiles of ion thermal transport coefficient (χ_i) and impurity particle transport coefficient (D_Z) obtained from simulations using MMM95 core transport model, with edge effective charge $Z_{eff,edge}$ of 1.4, 1.7, and 2.0, are shown.

Figure 9: Time evolution of central ion temperature, central helium density, radiative power loss and total alpha heating power obtained upon varying edge effective charge $Z_{eff,edge}$ are shown. The values are obtained from simulations using MMM95 core transport model, with $Z_{eff,edge}$ of 1.4, 1.7, and 2.0.

Figure 10: Time evolution of central ion temperature, central helium density, radiative power loss and total alpha heating power obtained upon varying line-averaged density (n_l) are shown. The values are obtained from simulations using MMM95 core transport model, with n_l of 0.8, 1.0, and $1.2 \times 10^{20} \text{ m}^{-3}$.

Figure 11: Time evolution of central ion temperature, central helium density, radiative power loss and total alpha heating

power obtained upon varying edge beryllium density to edge electron density ratio $n_{\text{Be,edge}}/n_{\text{e,edge}}$ are shown. The values are obtained from simulations using MMM95

core transport model, with $n_{\text{Be,edge}}/n_{\text{e,edge}}$ of 1%, 2%, and 3%.

Table 1 Notation used in this paper.

Symbol	Units	Description	Symbol	Units	Description
a	m	Plasma minor radius	χ_i	m^2/s	Ion thermal transport coefficient
r	m	Flux surface minor radius	χ_e	m^2/s	Electron thermal transport coefficient
R	m	Major radius to geometric center of each flux surface	χ_{Weiland}	m^2/s	Thermal transport coefficient calculated by Weiland model
ρ		Normalized minor radius	χ_{RB}	m^2/s	Thermal transport coefficient calculated from drift-resistive ballooning mode
$Z_{\text{eff,edge}}$		Effective charge at the edge	χ_{KB}	m^2/s	Thermal transport coefficient calculated from kinetic ballooning mode
κ_{95}		Plasma elongation at 95% flux surface	χ^{B}	m^2/s	Thermal transport coefficient with Bohm scaling
δ_{95}		Plasma triangularity at 95% flux surface	χ^{gB}	m^2/s	Thermal transport coefficient with gyro-Bohm scaling
B_{T}	Tesla	Vacuum toroidal magnetic field at R	D_{H}	m^2/s	Hydrogenic transport coefficient
B_{ϕ}	Tesla	Toroidal magnetic field	D_{Z}	m^2/s	Impurity transport coefficient
$\beta_{\text{0,ped}}$	Tesla	Normalized pedestal pressure	T_{ped}	keV	Pedestal temperature
s		Magnetic shear	T_i	keV	Ion temperature
I_{p}	MA	Plasma current	$T_{i,o}$	keV	Central ion temperature
q		Safety factor	T_e	keV	Electron temperature
ρ_s	m	Ion gyro-radius	$T_{e,o}$	keV	Central electron temperature
c_s	m/s	Speed of sound	n_l	10^{20} m^{-3}	Line-averaged density
p	Pa	Plasma pressure	n_{ped}	10^{20} m^{-3}	Pedestal density
p_e	Pa	Electron pressure	n_i	10^{19} m^{-3}	Ion density
μ_0	Hm^{-1}	Permeability of free space	n_e	10^{19} m^{-3}	Electron density
α		Normalized pressure gradient	n_{D}	10^{19} m^{-3}	Deuterium density
α_c		Normalized critical pressure gradient of ballooning mode	n_{T}	10^{19} m^{-3}	Tritium density
C_{imp}		Constant multiplied to the impurity transport coefficient	n_{He}	10^{18} m^{-3}	Helium density
			n_{Be}	10^{18} m^{-3}	Beryllium density
P_{rad}	MW	Radiative power loss	$P_{\alpha,\text{total}}$	MW	Total alpha heating power

Table 2 Summary of plasma properties obtained from simulations using Mixed B/gB core transport model, coupled with pedestal width model based on magnetic and flow shear stabilization, flow shear stabilization, and normalized poloidal pressure scalings.

Δ scaling	Time (s)	$T_{i,o}$ (keV)	$T_{e,o}$ (keV)	(10^{19} m^{-3})	T_{ped} (keV)	(10^{19} m^{-3})	$P_{\alpha,\text{total}}$ (MW)
$\Delta \propto \rho s^2$	10	3.83	5.06	4.89	0.70	3.68	0.31
	100	9.24	10.14	10.83	2.65	7.90	12.01
	1000	16.97	17.73	10.84	2.65	7.94	29.48
	3000	17.02	17.69	10.83	2.65	7.94	29.88
$\Delta \propto \sqrt{\rho R q}$	10	3.83	5.06	4.89	0.70	3.68	0.35
	100	9.00	9.91	10.80	2.46	7.89	10.52
	1000	16.50	17.21	10.85	2.47	7.95	27.32
	3000	16.72	17.43	10.87	2.46	7.91	27.50

Table 2 Summary of plasma properties obtained from simulations using Mixed B/gB core transport model, coupled with pedestal width model based on magnetic and flow shear stabilization, flow shear stabilization, and normalized poloidal pressure scalings. (Cont.)

Δ scaling	Time (s)	$T_{i,o}$ (keV)	$T_{e,o}$ (keV)	$n_{e,o}$ (10^{19} m^{-3})	T_{ped} (keV)	$n_{e,ped}$ (10^{19} m^{-3})	$P_{\alpha,total}$ (MW)
$\Delta \propto R\sqrt{\beta_{0,ped}}$	10	4.57	6.00	4.93	1.06	3.63	0.53
	100	9.52	10.46	10.78	2.88	7.89	13.88
	1000	17.36	18.03	10.79	2.88	7.96	32.21
	3000	17.58	18.26	10.82	2.88	7.94	32.83

Table 3 Summary of plasma properties obtained from simulations using MMM95 core transport model, coupled with pedestal width model based on magnetic and flow shear stabilization, flow shear stabilization, and normalized poloidal pressure scalings.

Δ scaling	Time (s)	$T_{i,o}$ (keV)	$T_{e,o}$ (keV)	$n_{e,o}$ (10^{19} m^{-3})	T_{ped} (keV)	$n_{e,ped}$ (10^{19} m^{-3})	$P_{\alpha,total}$ (MW)
$\Delta \propto \rho s^2$	10	7.12	9.72	4.89	0.72	3.49	1.07
	100	13.16	15.50	10.56	2.58	7.97	31.06
	1000	23.11	25.01	9.90	2.71	7.82	58.43
	3000	24.00	25.82	9.69	2.71	7.83	59.59
$\Delta \propto \sqrt{\rho Rq}$	10	7.20	9.80	4.87	0.73	3.49	1.15
	100	13.16	15.46	10.57	2.47	7.97	31.23
	1000	23.09	25.13	9.83	2.60	7.79	57.83
	3000	24.72	25.94	9.54	2.62	7.81	59.36
$\Delta \propto R\sqrt{\beta_{0,ped}}$	10	7.20	9.80	4.87	0.73	3.49	1.15
	100	13.13	15.52	10.55	2.57	8.02	31.04
	1000	23.13	25.39	9.95	2.88	7.85	61.13
	3000	24.68	26.35	9.83	2.90	7.85	61.84

Table 4 Quasi-steady state values of central ion and electron temperatures, and densities of ion, electron, deuterium, tritium, helium and beryllium. The values are taken from simulations without sawtooth oscillation, and simulations with sawtooth oscillation before and during sawtooth crash. Mixed B/gB core transport model is used.

	$T_{i,o}$ (keV)	$T_{e,o}$ (keV)	$n_{i,o}$ (10^{19} m^{-3})	$n_{e,o}$ (10^{19} m^{-3})
Without sawtooth oscillation	16.501	17.290	9.368	10.844
With,Before sawtooth crash	7.066	7.341	9.312	10.639
With,During sawtooth crash	6.907	7.213	9.299	10.620
% change	2.25	1.74	0.14	0.18
	$n_{D,o}$ (10^{19} m^{-3})	$n_{T,o}$ (10^{19} m^{-3})	$n_{He,o}$ (10^{18} m^{-3})	$n_{Be,o}$ (10^{18} m^{-3})
Without sawtooth oscillation	4.413	4.434	7.603	2.151
With,Before sawtooth crash	4.361	4.061	6.821	2.074
With,During sawtooth crash	4.355	4.062	6.826	2.070
% change	0.14	0.02	0.07	0.19

Table 5 Quasi-steady state values of central ion and electron temperatures, and densities of ion, electron, deuterium, tritium, helium and beryllium. The values are taken from simulations without sawtooth oscillation, and simulations with sawtooth oscillation before and during sawtooth crash. MMM95 core transport model is used.

	$T_{i,o}$ (keV)	$T_{e,o}$ (keV)	$n_{i,o}$ (10^{19} m^{-3})	$n_{e,o}$ (10^{19} m^{-3})
Without sawtooth oscillation	21.847	24.472	8.481	10.084
With,Before sawtooth crash	16.987	19.784	9.194	10.760
With,During sawtooth crash	11.600	12.212	8.944	10.327
% change	31.71	38.27	2.72	4.02

Table 5 Quasi-steady state values of central ion and electron temperatures, and densities of ion, electron, deuterium, tritium, helium and beryllium. The values are taken from simulations without sawtooth oscillation, and simulations with sawtooth oscillation before and during sawtooth crash. MMM95 core transport model is used. (Cont.)

	$n_{D,o}$ (10^{19} m^{-3})	$n_{T,o}$ (10^{19} m^{-3})	$n_{He,o}$ (10^{18} m^{-3})	$n_{Be,o}$ (10^{18} m^{-3})
Without sawtooth oscillation	4.014	3.519	8.449	2.223
With, Before sawtooth crash	4.265	3.8918	8.1165	2.262
With, During sawtooth crash	4.134	3.8922	8.1177	2.086
% change	3.07	0.010	0.015	7.78

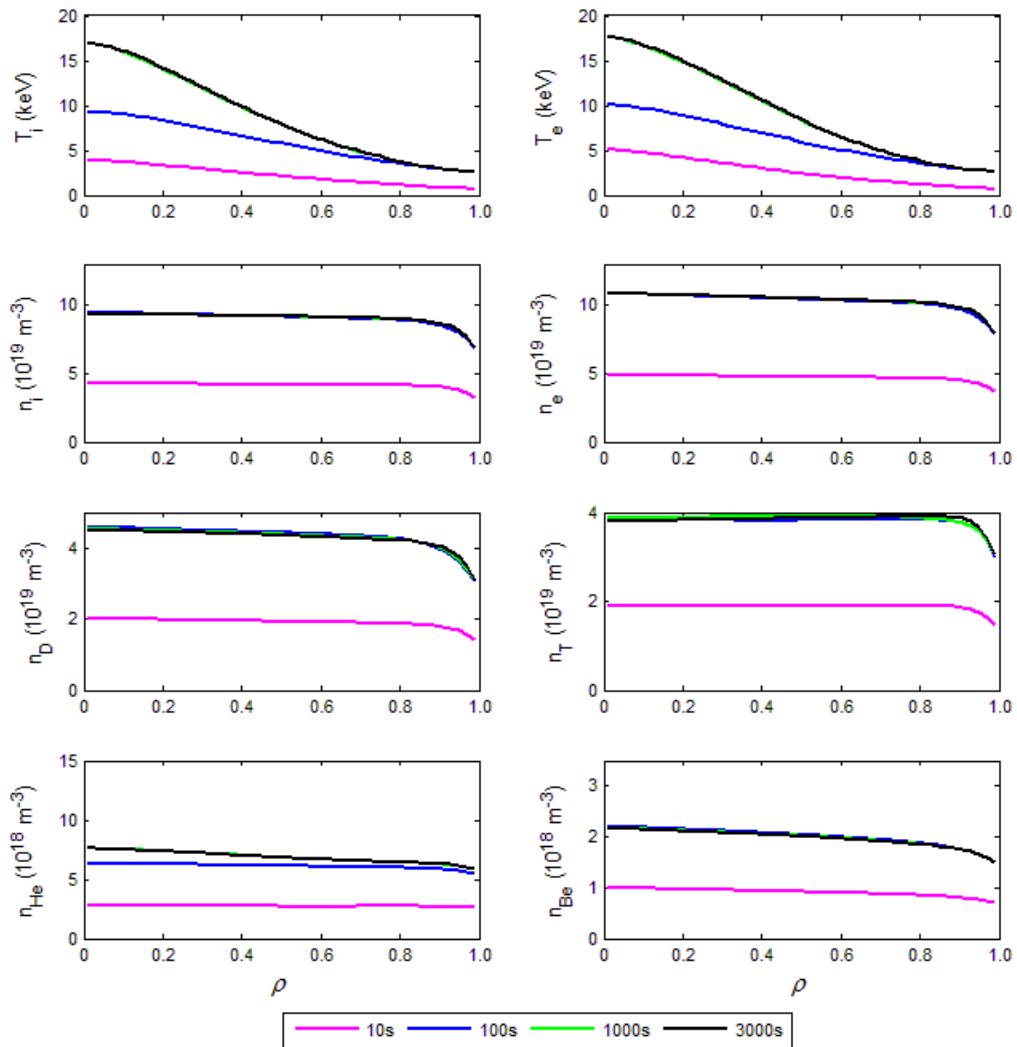


Figure 1 Profiles of ion and electron temperatures, and densities of ion, electron, deuterium, tritium, helium and beryllium at 10, 100, 1000, and 3000 sec. The profiles are obtained from simulations using Mixed B/gB core transport model.

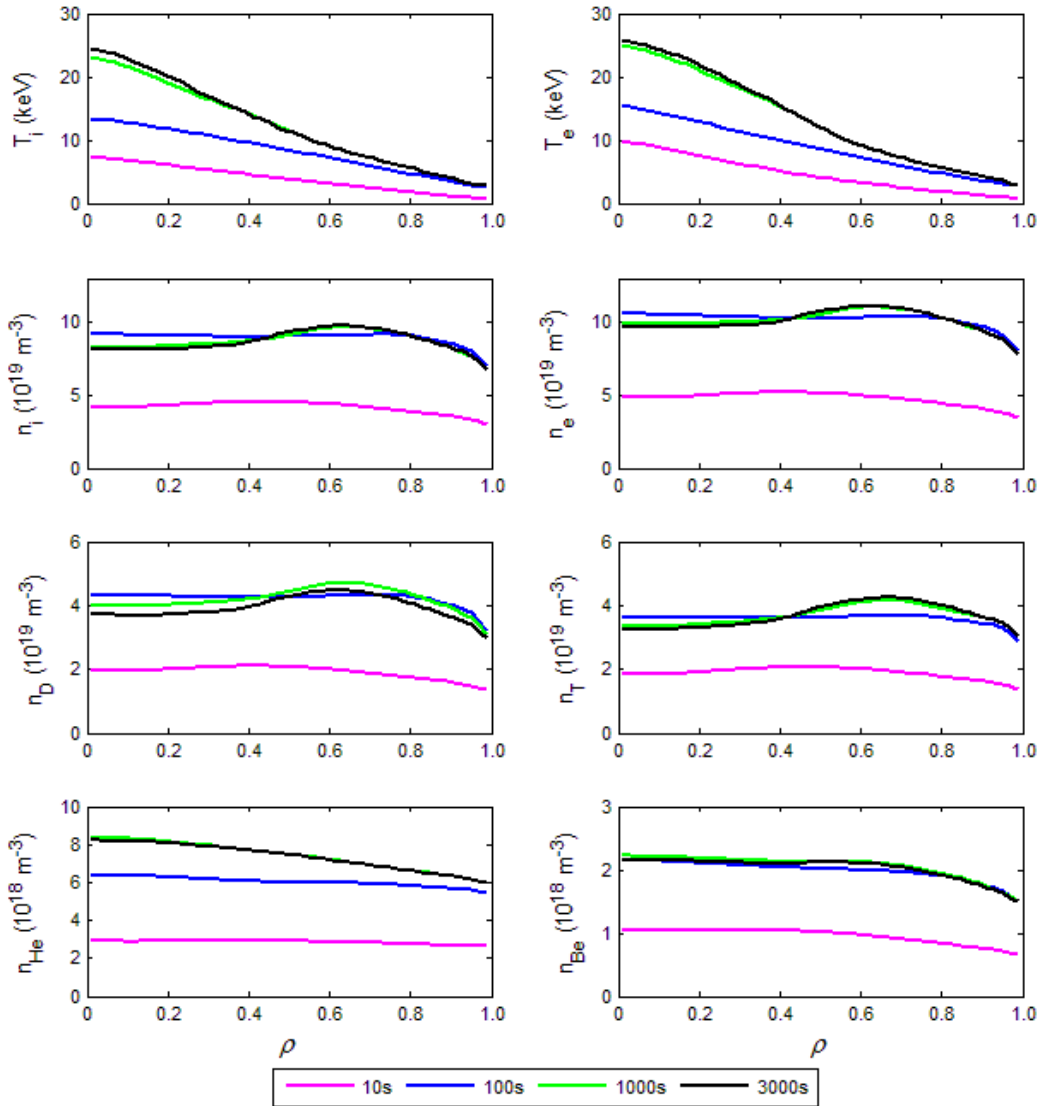


Figure 2 Profiles of ion and electron temperatures, and densities of ion, electron, deuterium, tritium, helium and beryllium at 10, 100, 1000, and 3000 sec. The profiles are obtained from simulations using MMM95 core transport model.

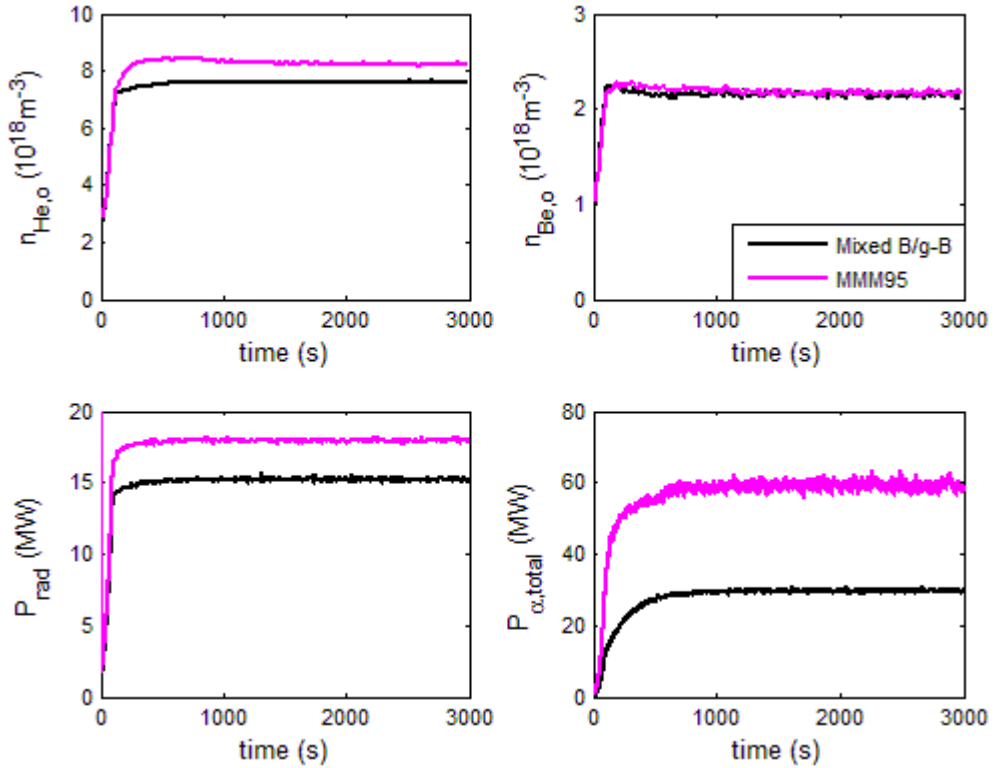
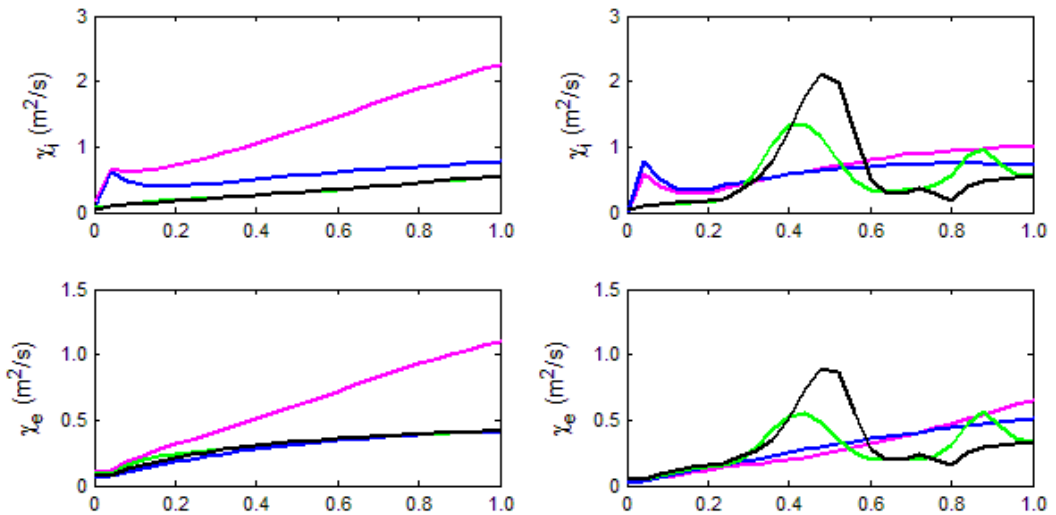


Figure 3 Time evolution of central helium and beryllium densities, radiative power loss and total alpha heating power are shown. The results are obtained from the simulations using either Mixed B/gB or MMM95 core transport models.



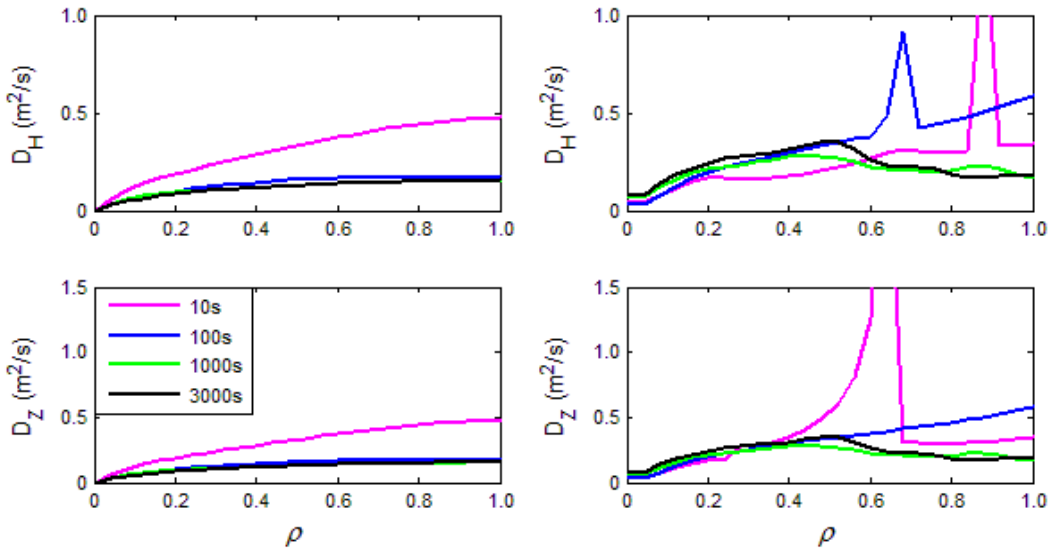


Figure 4 Profiles of ion and electron thermal transport coefficients (χ_i and χ_e), and hydrogenic and impurity transport coefficients (D_H and D_Z) obtained from Mixed B/gB (left panels) and MMM95 (right panels) core transport models are shown.

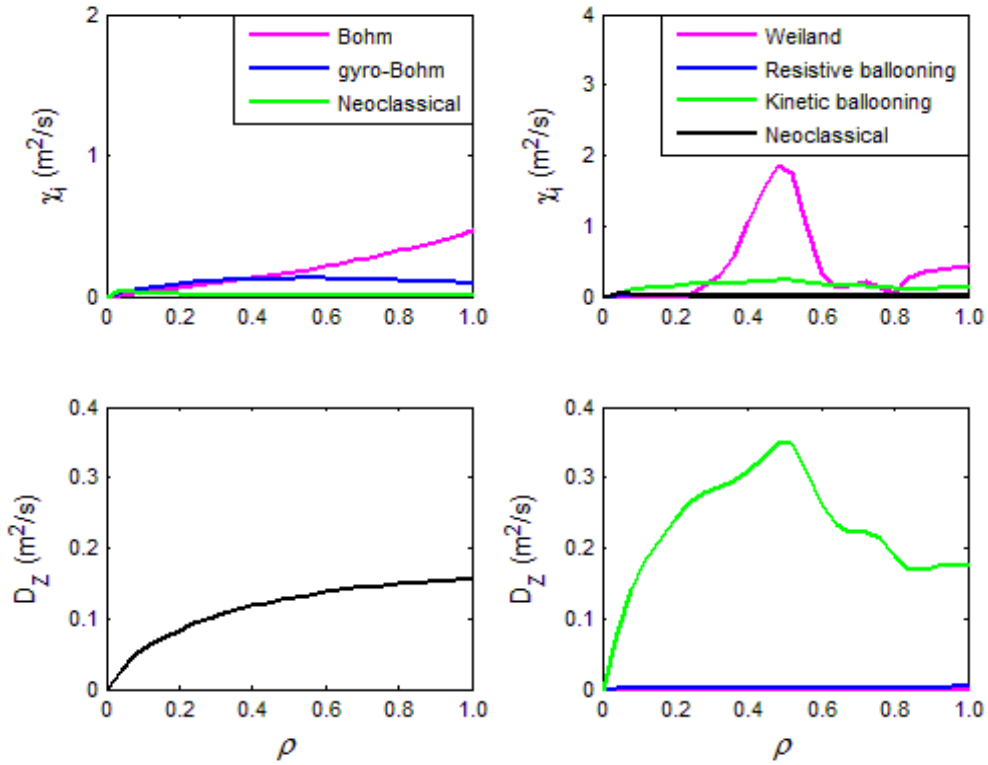


Figure 5 Contributing terms in ion thermal transport coefficients (χ_i) and impurity particle transport coefficient (D_Z) calculated using Mixed B/gB and MMM95 core transport models are shown as functions of normalized minor radius.

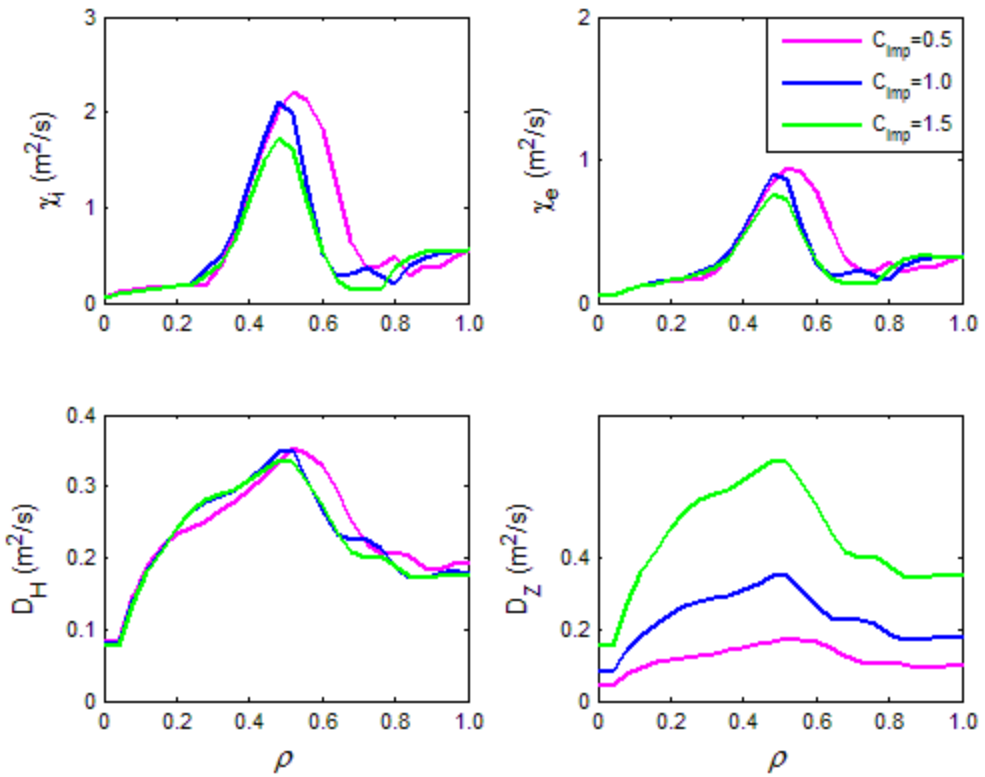
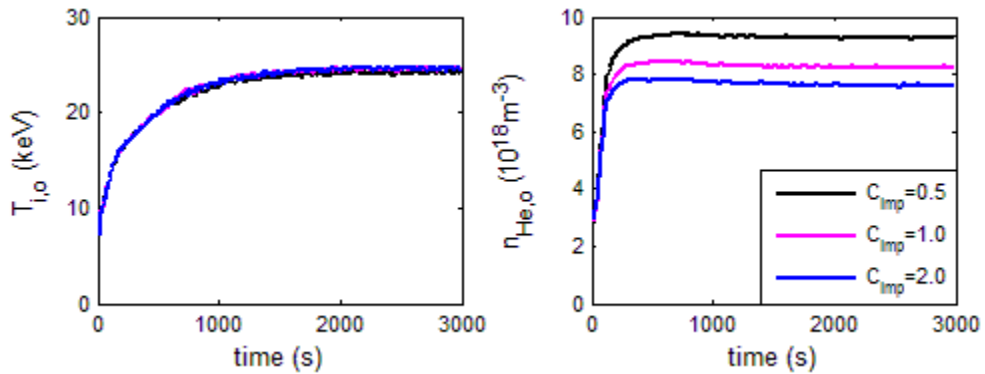


Figure 6 Profiles of ion and electron thermal transport coefficients (χ_i and χ_e), and hydrogenic and impurity particle transport coefficients (D_H and D_Z) obtained from simulations using Mixed B/gB and MMM95 core transport models, with $C_{imp}= 0.5, 1.0, 2.0$, are shown.



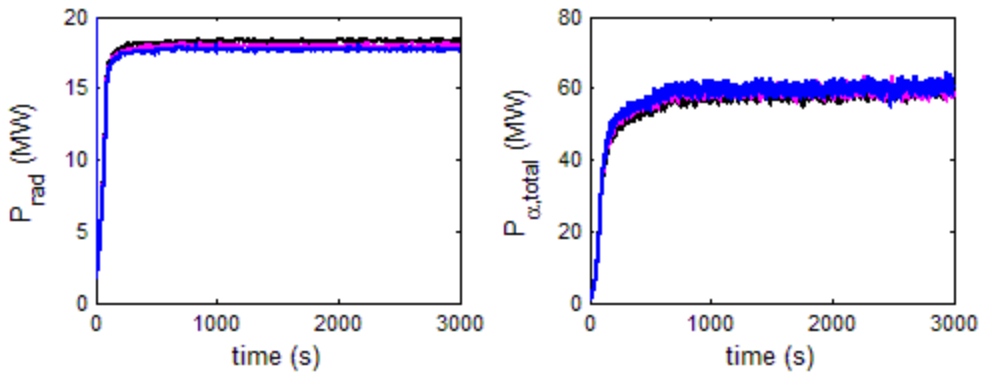


Figure 7 Time evolution of central ion temperature, central helium density, radiative power loss and total alpha heating power upon varying the constant C_{imp} are shown. The results are obtained from simulations using MMM95 core transport model, with C_{imp} of 0.5, 1.0, and 2.0.

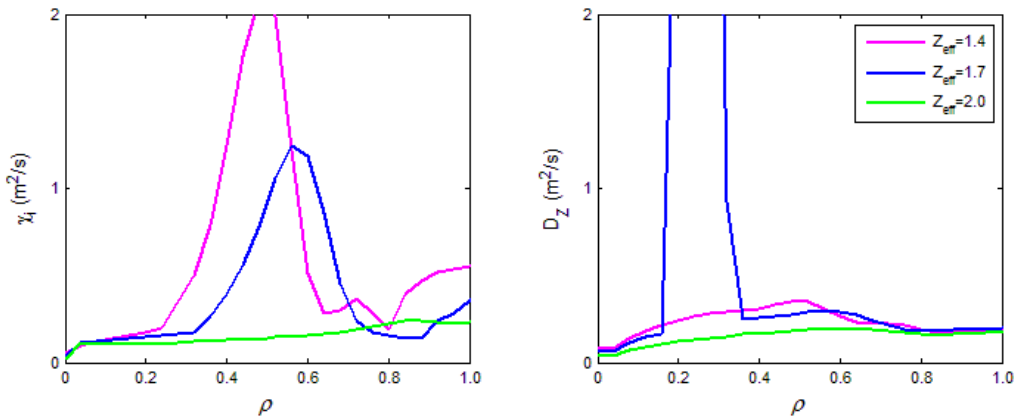
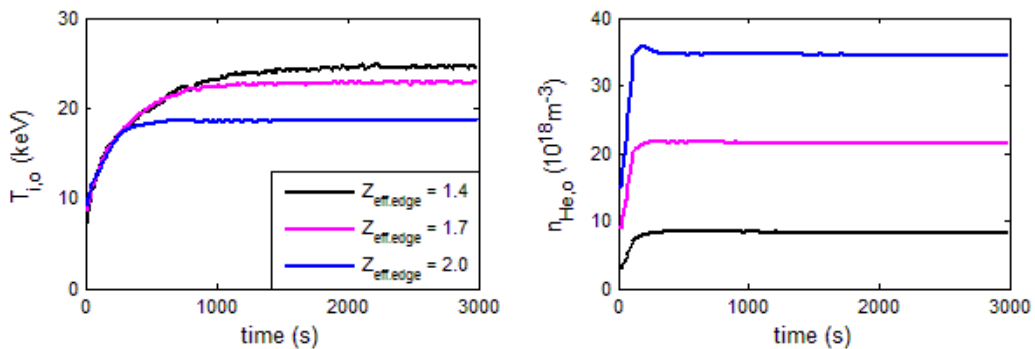


Figure 8 Profiles of ion thermal transport coefficient (χ_i) and impurity particle transport coefficient (D_Z) obtained from simulations using MMM95 core transport model, with edge effective charge $Z_{eff,edge}$ of 1.4, 1.7, and 2.0, are shown.



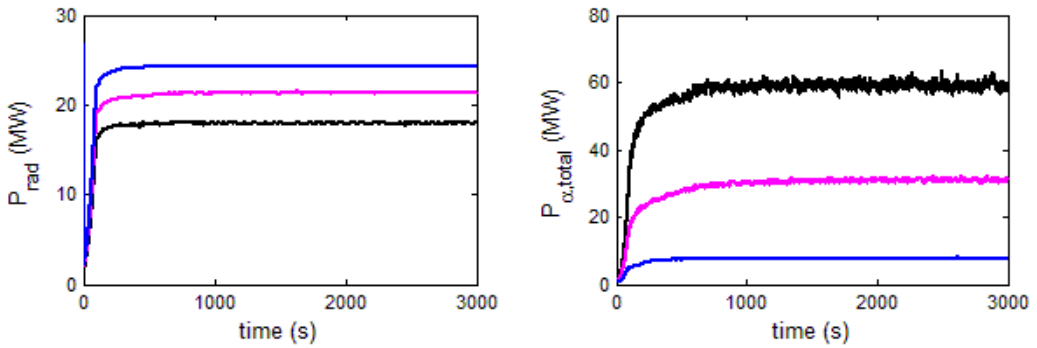


Figure 9 Time evolution of central ion temperature, central helium density, radiative power loss and total alpha heating power obtained upon varying edge effective charge $Z_{\text{eff,edge}}$ are shown. The values are obtained from simulations using MMM95 core transport model, with $Z_{\text{eff,edge}}$ of 1.4, 1.7, and 2.0.

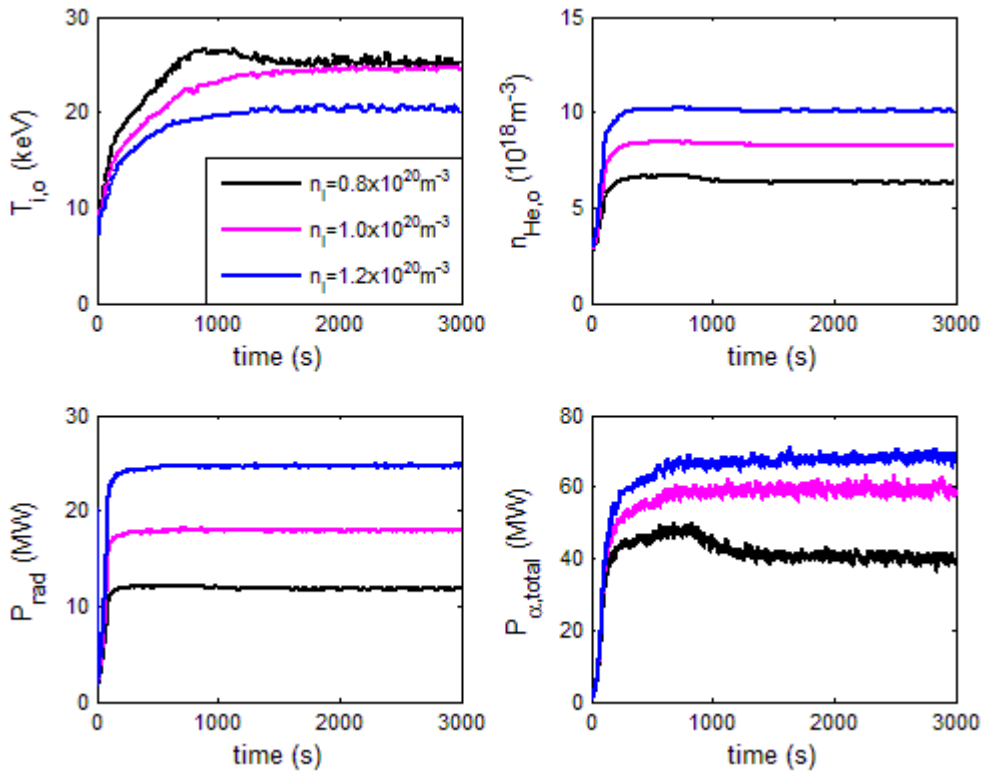


Figure 10 Time evolution of central ion temperature, central helium density, radiative power loss, and total alpha heating power obtained upon varying line-averaged density (n_i) are shown. The values are obtained from simulations using MMM95 core transport model, with n_i of 0.8, 1.0, and $1.2 \times 10^{20} \text{ m}^{-3}$.

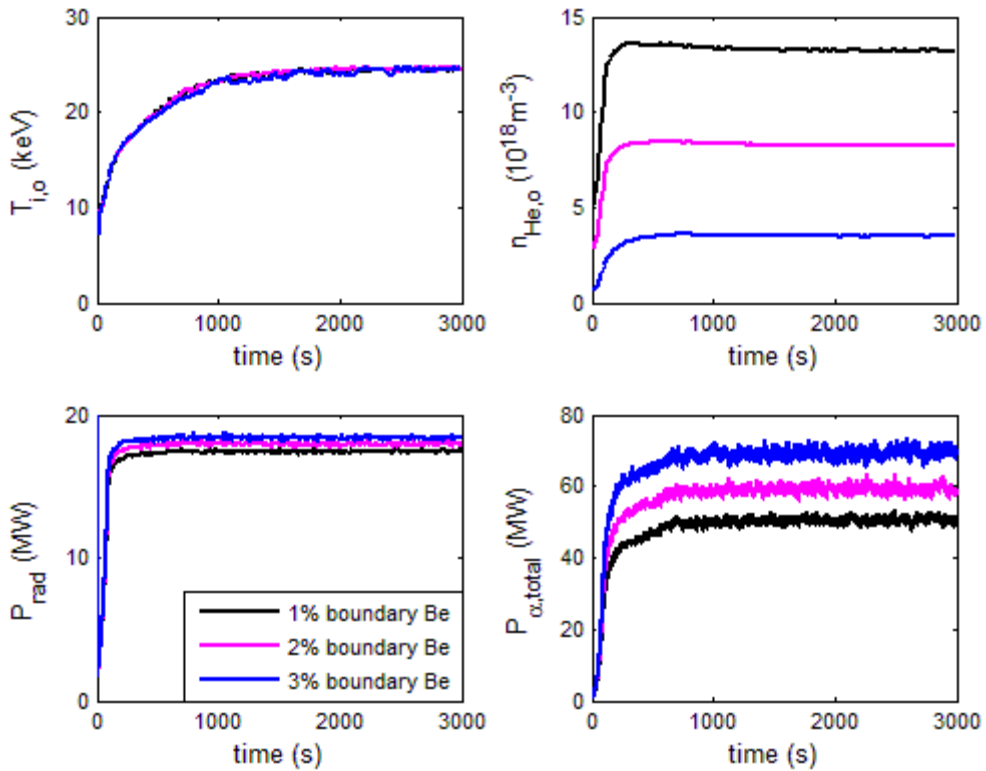


Figure 11 Time evolution of central ion temperature, central helium density, radiative power loss, and total alpha heating power obtained upon varying edge beryllium density to edge electron density ratio $n_{Be,edge}/n_{e,edge}$ are shown. The values are obtained from simulations using MMM95 core transport model, with $n_{Be,edge}/n_{e,edge}$ of 1%, 2%, and 3%.